Hyperfine structure and isotope shifts of xenon measured for near-infrared transitions with Doppler-free saturated absorption spectroscopy

James Bounds[1], Alexandre Kolomenskii[1], Rusty Trainham[2], Manuel Manard[2], Hans Schuessler[1]

[1]Department of Physics and Astronomy, Texas A&M University, College Station, Texas 77843-4242, USA
[2] Special Technologies Laboratory, Mission Support and Test Services, 5520 Ekwill St., Santa Barbara, CA 93111, USA

ABSTRACT

Hyperfine structure and isotope shifts of Xe were investigated with Doppler-free saturated absorption spectroscopy for all transitions in the 820-841nm spectral interval. The Xe samples were commercial gases of natural isotopic abundances. The measurements were performed by employing a widely tunable narrow line Ti:sapphire laser. The hyperfine structures for ^{129}Xe and ^{131}Xe were well resolved. For the transitions with the wavelengths in vacuum near 820.860nm and 841.150nm also isotope shifts of the even isotopes were clearly observed. The modeling of the shapes of the observed absorption lines qualitatively reproduces experimental spectral profiles. The measured absorption peaks of the hyperfine structure and isotope shifts of Xe isotopes present characteristic spectral fingerprints for their identification. Eventually, quantitative spectral analysis will provide isotopic abundances of natural, as well as radioactive Xe gas samples.

Keywords: Saturated absorption spectroscopy, High resolution Doppler-free spectroscopy, Hyperfine structure, Isotope shifts, Xe isotopes

I. INTRODUCTION

The hyperfine structure (HFS) in atomic spectra originates from the splitting of the fine structure lines due to interaction of the nuclear magnetic moment with the magnetic field produced by electrons as well as due to coupling of the nuclear electric quadrupole with the gradient of the electric field [1]. Isotopes of xenon with an odd number of nucleons (^{129}Xe and ^{131}Xe) have nonzero magnetic moments and electric quadrupoles resulting in significant splitting of HFS lines. Consequently, measurements of HFS give information on nuclear spins, moments and charge distribution. Since the energy splitting of HFS is typically of the order of 1GHz or less, the relative variations of the frequency and wavelength that should be measured with the near-IR +transitions with typical frequencies f~3.8x10^{14}Hz (for λ~800 nm) are of the order of ~2.8x10^{-6} and less. Such measurements require high resolution spectroscopic techniques. The main limitation comes from the Doppler broadening due to thermal motion of atoms, which for room temperature with typical velocities of atoms v~200m/s (for Xe) gives relative spectral broadening $\sim(v/c)$~0.7x10^{-6}. Thus, for a straightforward spectroscopic measurement the Doppler broadening will conceal finer features of the HFS. The same holds for the isotope shifts (ISs), which usually are even smaller than the HFS splitting. Doppler-free saturation spectroscopy [2] (related to the Lamb-dip effect [3]) was designed to overcome this limitation. Since HFS is specific to a certain isotope, its experimental observation is indicative to the presence of this isotope. Xenon (Z=54) has seven stable isotopes with various natural abundances (^{126}Xe: 0.0089%, ^{128}Xe: 1.92%, ^{129}Xe: 26.4%, ^{130}Xe: 4.1%, ^{131}Xe: 21.2%, ^{132}Xe: 26.9%, ^{134}Xe: 10.4%) and two very long lived isotopes (^{124}Xe: 0.0096%, 1.8x10^{22} yr; ^{136}Xe: 8.9%, 2.165 × 10^{21} yr, which for practical applications can be also considered as stable), as well as the short lived radioactive isotopes (^{131m}Xe, 11.9d; ^{133m}Xe, 2.19d; ^{133}Xe, 5.24d; ^{135}Xe, 9.10h), which are of interest in the detection of nuclear testing. Xe is a trace gas in the atmospheric air with concentration of about 0.086ppm [4]. Two odd isotopes exhibit a hyperfine structure since they have nonzero nuclear spin (^{129}Xe: I = 1/2 and ^{131}Xe: I = 3/2), while ^{136}Xe is a magic nucleus with closed shells and 82 neutrons. Measurements of the relative isotopic abundances of Xe gas can be used for highly sensitive detection of underground or underwater nuclear explosions [5], for astrophysical research, in particular dating of meteorites [6], for atmospheric studies [7] and in medicine [8].

This work was done by Mission Support and Test Services, LLC, under Contract No. DE-NA0003624 with the U.S. Department of Energy, the Office of Defense Programs, and supported by the Site-Directed Research and Development Program. DOE/NV/03624--1594.

The spectroscopic information contained in HFS and IS provides data on the atomic nucleus structure (charge radius, magnetic and quadrupole moments) and its interactions with the surrounding electronic shells, and also helps in verification of calculational models [9-11]. Being of significant interest for comparison of theory with experimental observations, different 6s-6p transitions were investigated by a variety of experimental methods. In earlier works [12,13] an interferometric approach was used. Hyperfine structures of the $5p^5 6s\,^3P_2$ state of Xe^{129} and Xe^{131} were measured by the atomic beam nuclear magnetic resonance method with high precision (to 10^{-8}) [14]. Precise measurements of Xe isotopes for the transition from the $5p^5 6s\,[3/2]_2$ metastable atomic state to $5p^5 6p\,[3/2]_2$ at ~823nm were performed using a collisional ionization scheme and also fluorescence detection in collinear laser spectroscopy [15,16], which allowed evaluation of isotope shifts and variations of the charge radii. Narrow spectral emission from diode lasers, typically realized with an optical feedback stabilization technique, was employed with Doppler-free saturated absorption spectroscopy for studying HFS of Xe for transitions near different wavelengths (in nm): 820, 823, 828, 834 [17]; 820, 823 [18]; 820, 823, 826, 828 [19]; 820, 823, 828, 834, 841 [20]; 828, 834 [21]; 823 [22].

In this work we employed Doppler-free saturated absorption spectroscopy with a broadly tunable narrow-line Ti:sapphire laser to resolve HFS spectra of Xe for all near-IR transitions of the 6ns-6np series in the 820-841nm spectral interval. We observed Xe hyperfine structure in an inductively created discharge with saturation spectroscopy, which overcomes the Doppler broadening and resolves separate lines within the HFS multiplets. The measured spectra allowed to evaluate the HFS constants, which were verified by comparison with previously determined values. The motivation for this work was twofold: first, to measure with the same method of saturated absorption spectroscopy the spectra of the HFS and isotope shifts of all transitions of Xe in the spectral interval 820-841nm accessible with the Ti:sapphire laser, and second, to investigate the manifestation of specific features of different isotopes in these spectra.

The schematic of the investigated transitions is shown in Fig. 1, and the corresponding transition wavelengths in this figure and further in the text are given for vacuum. To obtain the wavelengths for air the indicated values should be multiplied by 0.999725. The transitions in Fig. 1 correspond to all transitions of the 6ns-6np series within the optical wavelength interval from 820 to 841nm. Three of these transitions (near 820, 828 and 841 nm) start from metastable levels, and therefore their signals can be expected to be enhanced relatively to other transitions. The starting 6s states of the studied transitions are ~8-9 eV above the Xe ground state ($4d^{10}5s^2 5p^6$, $^1S_0$), and therefore, attaining these states requires some source of excitation (optical with vacuum ultraviolet radiation [23], collisional ionization in a discharge [24], or excitation by an electron beam [25]). In this work we use an inductively created plasma in a rarefied Xe gas.

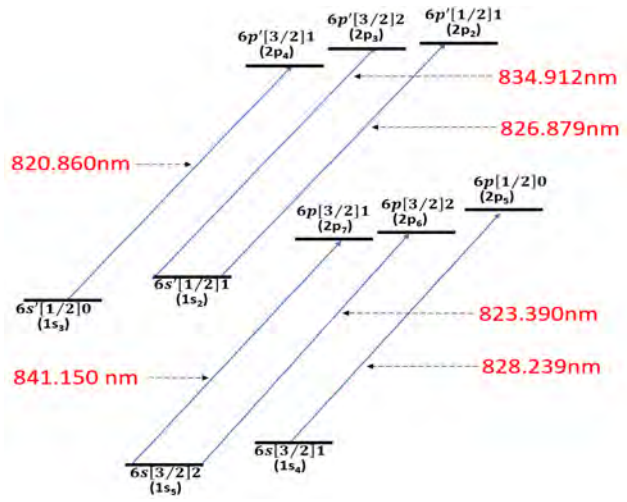

FIG. 1. Schematic of investigated transitions (wavelengths of transitions are given for vacuum). The levels are given in Racah and Paschen notations (the latter in parentheses).

The excited Xe atomic system can be presented as a core ion plus an electron, and the following coupling scheme can be used [25]. The parent ion core has terms $^2P_{1/2}$ or $^2P_{3/2}$ and, as is commonly accepted, the $P_{1/2}$ state is labelled with "prime"). The spin (s_1) - orbit (l_1) interaction in the ion is large resulting in the orbital momentum j_1. The total orbital momentum j_1 of the core ion and the orbital momentum l_2 of the excited electron combine to form an angular momentum K. The spin of the excited electron s_2 then interacts with the angular momentum K to form the resultant angular momentum quantum number J (i.e. $J = K \pm ½$). Thus, the excited states are conveniently described by Racah notation: $nl_2[K]J$, where n and l_2 are the principal and orbital quantum numbers of the excited electron. Paired nucleons have zero net spin because the spin vectors of nucleons in a pair tend to point in opposite directions. Since the charge for Xe is Z= 54, the number of protons is even. Of the nine stable isotopes of xenon, only two (^{129}Xe and ^{131}Xe) have an odd number of neutrons. Due to the coupling between the intrinsic electric and magnetic fields of the electrons and the atomic nucleus, the energies of the otherwise degenerate states in these isotopes shift slightly, leading to hyperfine structure.

II. THEORETICAL BACKGROUND

The hyperfine structure is determined by the interaction of the nuclear spin and quadrupole moment, respectively with the magnetic and electric fields induced by electrons. Since nuclei with a nuclear spin $I \geq 1/2$ can possess a magnetic moment, and the shell electrons in states with the total angular momentum $J \neq 0$ produce a magnetic field at the site of the nucleus, this gives rise to a dipole interaction energy [26-28]

$$W_D = -\mu B, \tag{1}$$

where μ is the nuclear magnetic moment and B is the magnetic field created by the electrons at the position of the nucleus. The magnetic field created by electrons is proportional to the angular momentum J, and the magnetic moment is proportional to the nuclear spin I, which results in the splitting of the energy levels by

$$\Delta E = A\, I \cdot J, \tag{2}$$

where the scalar product can be presented in the form

$$I \cdot J = (1/2)[F(F+1) - I(I+1) - J(J+1)]. \tag{3}$$

Nuclei with I = 0 and I=1/2 have a spherically symmetric charge distribution. Therefore, a non-zero electric quadrupole moment of the nucleus Q occurs only for an isotope with a nuclear spin greater than ½. The electric quadrupole moment of a nucleus with $I \geq 1$ interacts with an electric field gradient produced by the shell electrons in a state with $J \geq 1$ according to

$$W_Q = eQV_{zz}(0), \tag{4}$$

where e is the charge of an electron, and $V_{zz}(0) = \partial^2 V/\partial z^2|_{z=0}$ is the electric field gradient produced by the electrons at the position of the nucleus $z = 0$. For a particular atomic level characterized by an angular momentum quantum number J, the coupling with the nuclear spin I gives a new total angular momentum F according to the vector operator formula $\boldsymbol{F} = \boldsymbol{I} + \boldsymbol{J}$. For a nucleus with the angular momentum I, the possible values of the quantum number F representing the total angular momentum of the whole atomic system (nucleus plus electrons) are within the bounds $|I - J| \leq F \leq I + J$ and separated by integer steps from an upper limit of $J + I$ to a lower limit of $|J - I|$. Thus, the hyperfine interaction removes the degeneracy of different F levels and the number of possible F values is the smaller of $2J+1$ and $2I+1$ [4, 5]. Consequently, one obtains the expression for the hyperfine structure energies of all F levels of a hyperfine structure multiplet with respect to the atomic fine structure level J (see, e.g., [29]):

$$E_F = \frac{1}{2}\,AC \;+\; B\,\frac{(3/4)C(C+1) - I(I+1)J(J+1)}{2I(2I-1)J(2J-1)} \tag{5}$$

where

$$C = F(F + 1) - I(I + 1) - J(J + 1)$$

and

$$A = \frac{\mu B_e(0)}{I \cdot J}, B = eQV_{zz}(0). \quad (6)$$

Here $B(0)$ is the magnetic field created by electrons at the position of the nucleus. The allowed transitions follow the selection rules: $\Delta J = 1, \Delta F = \{0, \pm 1\}$, and for $F = 0, \Delta F = 0$ is prohibited. The relative strength $S_{F,F'}$ of the lines in the HFS multiplet can be calculated [30-32] assuming dipole transitions between atomic states (J,F,I)->(J',F',I)

$$S_{F,F'} = \frac{(2F + 1)(2F' + 1)}{(2I + 1)} \begin{Bmatrix} J & F & I \\ F' & J' & 1 \end{Bmatrix}^2, \quad (7)$$

where the factor in curly brackets is the Wigner 6-*j* symbol.

III. EXPERIMENTAL SETUP AND RESULTS OF HFS MEASUREMENTS

In order to accurately measure the hyperfine structure of Xe, thermal motions of Xe atoms in the measurement cell must be overcome, since Doppler broadening obscures closely spaced transition frequencies under normal conditions. This goal is accomplished via the method of Lamb-dip saturation spectroscopy [2]. The experiment is carried out in the configuration with counter-propagating pump and probe beams (Fig.2), where atoms having velocity vectors perpendicular to both beams preferentially contribute to the signal, thus cancelling out first-order Doppler shifts of transition frequencies.

We produce tunable narrow-line radiation for realization of the resonance excitation of Xe from the metastable 6s state to 6p state using a Coherent 899 Ti:sapphire ring laser actively stabilized to a temperature and pressure controlled external reference cavity. Fine wavelength scanning is provided by two synchronous galvo Brewster plates mounted inside the reference cavity and inside the laser cavity, respectively. A combination of two electronically adjustable intra-cavity etalons ensures single mode operation while providing feedback for cavity stabilization. Before engaging active stabilization, the center of the scan is coarsely set using a birefringent filter and then finely adjusted using an electronic offset to one of the intra-cavity etalons. All transitions exhibiting hyperfine structures within the spectral interval 820-841nm covered by this tunable Ti:sapphire laser have been investigated.

To isolate the signal arising from the saturation of the atomic transitions, a mechanical chopper is employed to modulate the pump beam which creates a corresponding modulation in the counter-propagating probe beam through saturation of the electronic transitions. A lock-in amplifier synchronized to the chopper frequency detects the probe beam modulation via a photodiode. The narrow-band detection of the lock-in gives good rejection of the laser intensity noise. A second lock-in amplifier detects the remaining pump beam exiting the xenon cell to give a straightforward absorption measurement.

The mode structure of the Ti: sapphire laser radiation is monitored with a Burleigh 1.5 GHz scanning Fabry-Perot etalon (resolution 0.01 cm^{-1}). A separate scanning Fabry-Perot etalon with a free spectral range of 2GHz provides fine frequency detuning information for the experimental scans. A commercial wavemeter (Burleigh WA-10) is used to set the center wavelength of the scanning region before engaging active stabilization of the laser. A separate homemade wavemeter of higher resolution is used after the laser is locked to the reference cavity to measure specific points in the scan. The combination of the high resolution wavemeter measurement and the data from the scanning Fabry-Perot etalon allows the scans to be calibrated in wavelength to a Zeeman-stabilized helium-neon laser.

The initial population of the 6s state is produced by an inductive discharge in a cell filled with Xe. The cell consists of a borosilicate glass cell (Thorlabs GCV251) fitted with an external high vacuum valve, which

allows pre-filling of Xe using a separate vacuum chamber and a vacuum gauge. The inductive discharge is maintained by six turns of 14-gauge wire terminated with a 50 ohm resistance to ground. A steady inductive discharge plasma is achieved with 0.02 mbar Xe pressure at the frequency of the driving RF field of ~175MHz with an RF power consumption of ~5W. Due to the low power and sub-optimal solenoid geometry, an external electric field provided by a handheld Tesla coil is required in order to initiate the plasma. Once started, the discharge is entirely maintained by the RF field.

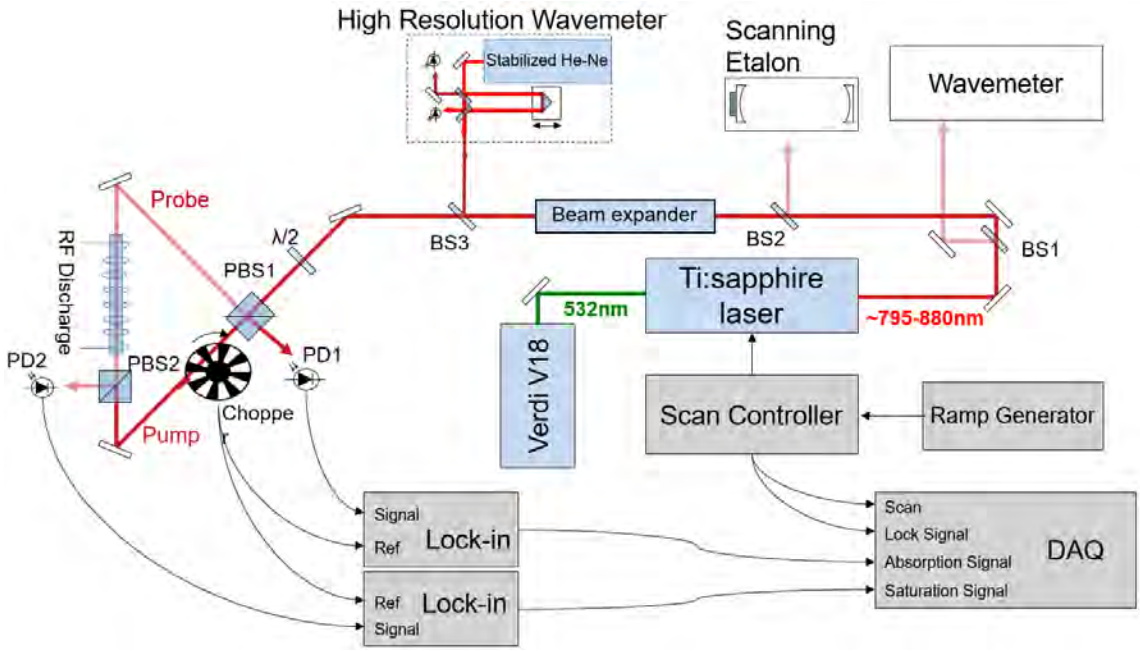

FIG. 2. Experimental setup for measuring the hyperfine structure of Xe. The Ti:sapphire (Coherent 899) laser is pumped using a frequency doubled Nd:YAG laser (Verdi V18). The output can be tuned roughly within 795-880nm, which is monitored using a wavemeter (Burleigh WA-10). A scanning Fabry-Perot etalon (FSR 2GHz) provides fine detuning information as the laser is scanned around a wavelength measured by a homemade high-resolution wavemeter. A beam expansion telescope is used for re-collimation and increasing the beam diameter in order to minimize transit-time broadening. The combination of a half waveplate and a polarizing beam splitter (PBS1) determines the intensities that are respectively coupled into the pump and probe beams. Additionally, PBS1 serves the purpose of re-directing light from the pump beam that exits the RF discharge cell into a photodiode (PD1) for measuring direct absorption. A second polarizing beam splitter (PBS2) directs light exiting the RF discharge cell from the probe beam into a photodiode (PD2) that is used for monitoring the saturation signal. The signals from both photodiodes are detected using two lock-in amplifiers which are both synchronized to a mechanical chopper operating on the pump beam.

HFS of the 6s′[1/2]0 → 6p′ [3/2]1 transition near 820.860nm

The starting level is metastable and does not have hyperfine splitting (Fig. 3). For ^{129}Xe: the lower state has *J=0, I=1/2* and the upper state *J=1, I =1/2*; for ^{131}Xe: the lower state has *J=0, I=3/2*, and the upper state *J=1, I =3/2*. Since lower level does not exhibit HFS, from the observed line splitting the HFS constants of the upper level can be directly derived [18]. As was reported [19,20], the Doppler broadening strongly masks the HFS, which according to Fig. 3 consists of two lines for ^{129}Xe and of three lines for ^{131}Xe. However, with the saturation spectroscopy we could resolve all these lines. In the experiment, both transitions of ^{129}Xe and transitions of ^{131}Xe were observed (for the *F=3/2 F'=3/2* transition the signal was very low). The measured spectrum shown in Fig. 3(c) presents the amplitude of the lock-in signal due to the absorption reduction of the probe beam induced by the pump radiation. As can be seen, the HFS is spread over a relatively large frequency

range of about 8GHz, and the spectrum of Fig3(c) was obtained by stitching together two scans at the signal maximum. A similar procedure was employed in Ref. [20]. The expected natural linewidth of this transition is 3.9MHz [18], while the observed width was about 10MHz. In a previous study [18] it was noted that the signal-to-noise ratio for this transition was too poor, however, populating the lower metastable state was quite efficient [19].

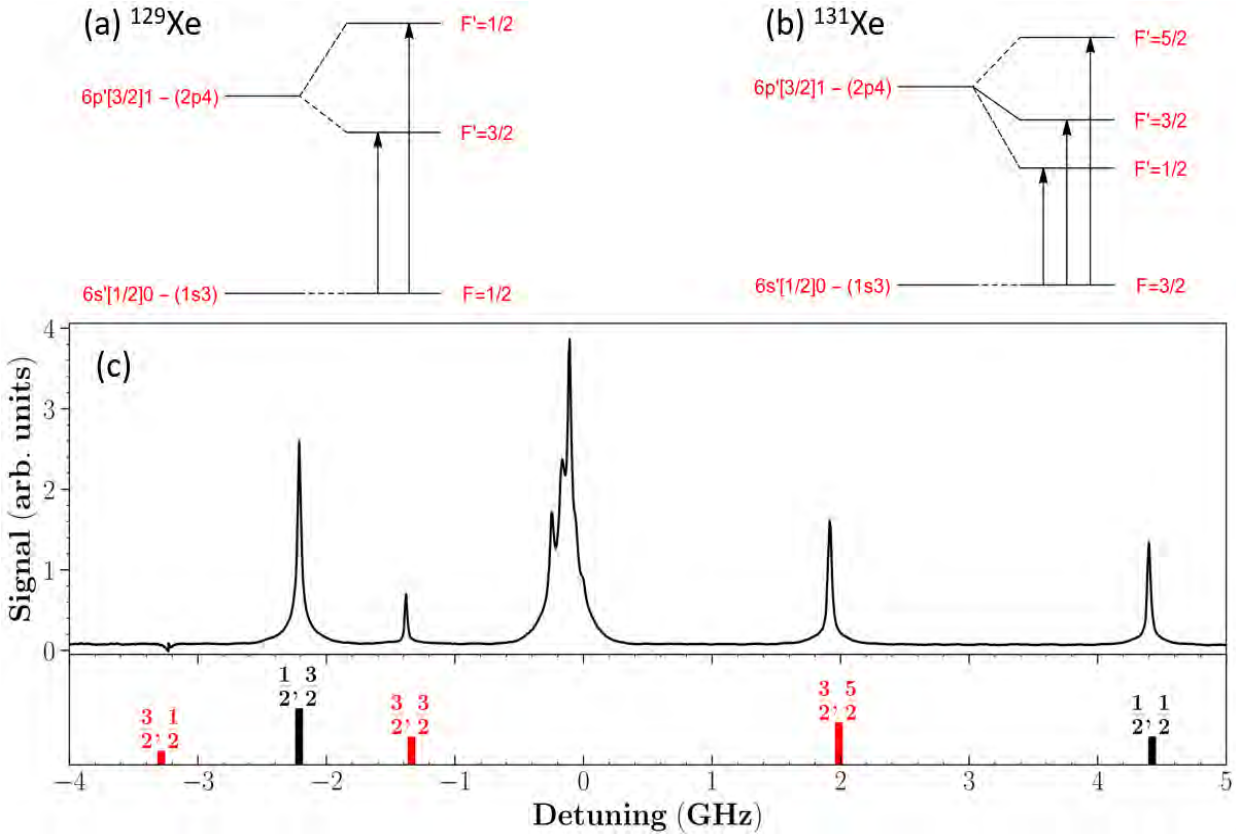

FIG. 3. Data for the $6s'[1/2]0 \rightarrow 6p[3/2]1$ transition near 820.860nm: (a),(b) Schematics of the HFS transitions for ^{129}Xe and ^{131}Xe, respectively. (c) Experimental spectrum measured as the saturation signal amplitude from the lock-in amplifier depicted as a function of detuning (upper plot) and the calculated positions of the ^{129}Xe (black) and ^{131}Xe (red) HFS spectral lines (lower plot). For each spectral line the pairs (F,F') of the corresponding transitions are indicated. The heights of the segments are proportional to the relative line strengths, as calculated with Eq. (7). The frequency scale in (c) gives the relative detuning from the centroid wavelength of ^{129}Xe HFS, and the central enlarged portion of this plot near zero detuning showing the peaks of the even isotopes is presented in Fig. 9(a) of Section IV, where the isotope shifts are discussed in more detail.

ISs for different even isotopes can be identified from the peaks observed in the vicinity of the zero detuning and are discussed further in more detail in Section 4 of this paper. The observed spectra were compared to the results of calculations, showing slight shifts of the experimental and calculated peak positions.

For the calculations the HFS constants A and B were used for different states, as indicated in Table 1. Using the constants of Table 1 the lines of the HFS for different transitions were calculated using Eq. (5). Although the saturation signal is nonlinear, being the result of absorption of the probe beam during its

propagation in the gas, a certain correlation of the observed peak heights with the calculated strength of the HFS lines can be seen.

HFS of the 6s[3/2]2 → 6p[3/2]2 transition near 823.390nm

The level diagram of the transitions is shown in Fig. 4(a,b). Doppler-free lines with sharp peaks resulting from the Lamb-dip effect can be clearly seen in the plot of the measured spectrum (Fig. 4(c)). The plot in Fig. 4(d) shows the direct absorption signal of the pump beam with Doppler broadened dips corresponding to the resonant absorption lines.

Calculation of the HFS constants for ^{129}Xe and ^{131}Xe can be performed using observed HFS peaks for each of these isotopes. Briefly, the procedure is as follows. The frequencies of the HFS lines are expressed using Eq. (5) through the

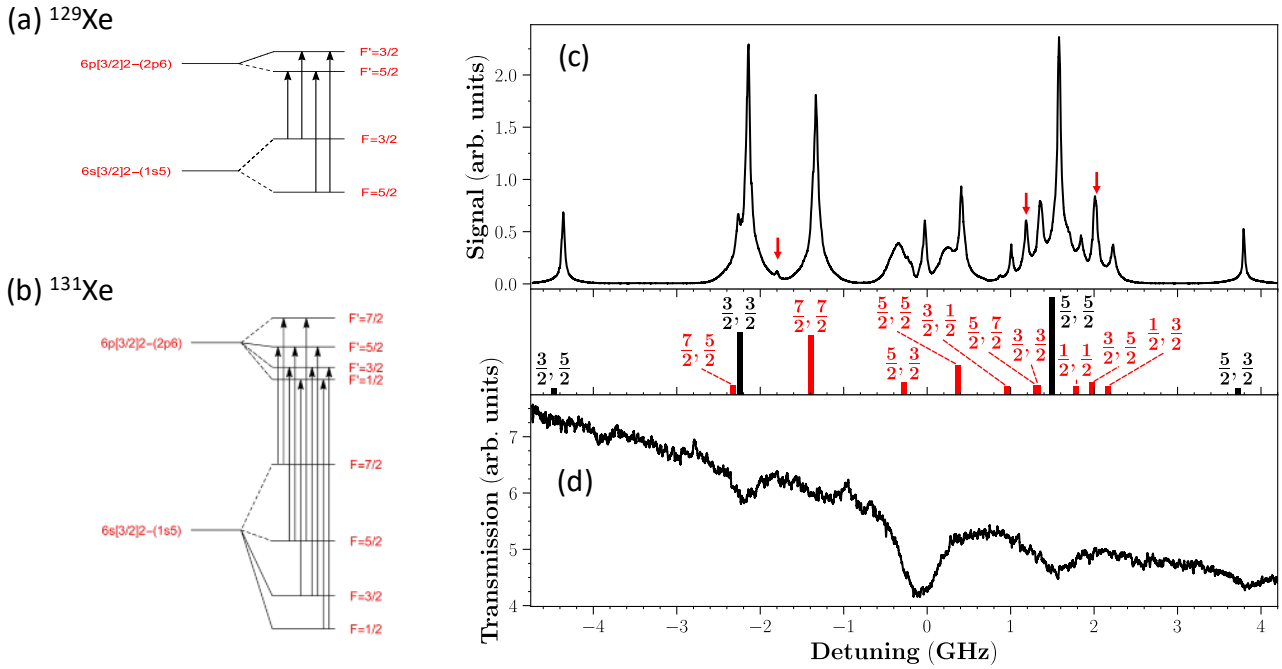

FIG. 4. (a,b) The schemes of the HFS for the 6s[3/2]2 → 6p[3/2]2 transition near 823.390nm for ^{129}Xe and ^{131}Xe, respectively. (c) Measured Xe spectrum (upper plot) and the calculated positions and strengths of the ^{129}Xe (black) and ^{131}Xe (red) HFS spectral lines (lower plot). The heights of the segments are proportional to the relative line strengths, as calculated with Eq. (7). Red arrows indicate artifacts due to crossover signals resulting from the close spacing of ^{131}Xe levels sharing a common lower level. (d) The direct absorption signal of the pump beam.

unknown HFS constants A_1 and B_1 for the lower level and A_2 and B_2 of the upper level. The shift of the spectral position of the centroid of the HFS also is considered as unknown. Then by minimizing the root-mean-square deviation of the calculated and experimental values the unknown constants $A_{1,2}$ and $B_{1,2}$ can be determined. The experimentally determined constants are presented further in Table 1.

It should be noted that the signal in Fig.4(c) from the even isotopes was suppressed due to strong absorption and saturation. Consequently, there is only a small peak in the center region where a large absorption occurs, as comparison of (c) and (d) in Fig. 4 shows. Additionally, this small peak is accompanied by some side lobes. This type of a peak shape appears in our numerical model of the saturation signal presented

in Section 5, which confirms that the cause of this peak suppression is the large optical depth, originating in this case from the strong absorption of even isotopes in this spectral region.

HFS of the $6s'[1/2]1 \rightarrow 6p'[1/2]1$ transition near 826.879nm

The schematics for the HFS transitions near 826.879nm for ^{129}Xe and ^{131}Xe isotopes and the experimentally measured spectrum are shown in Fig. 5.

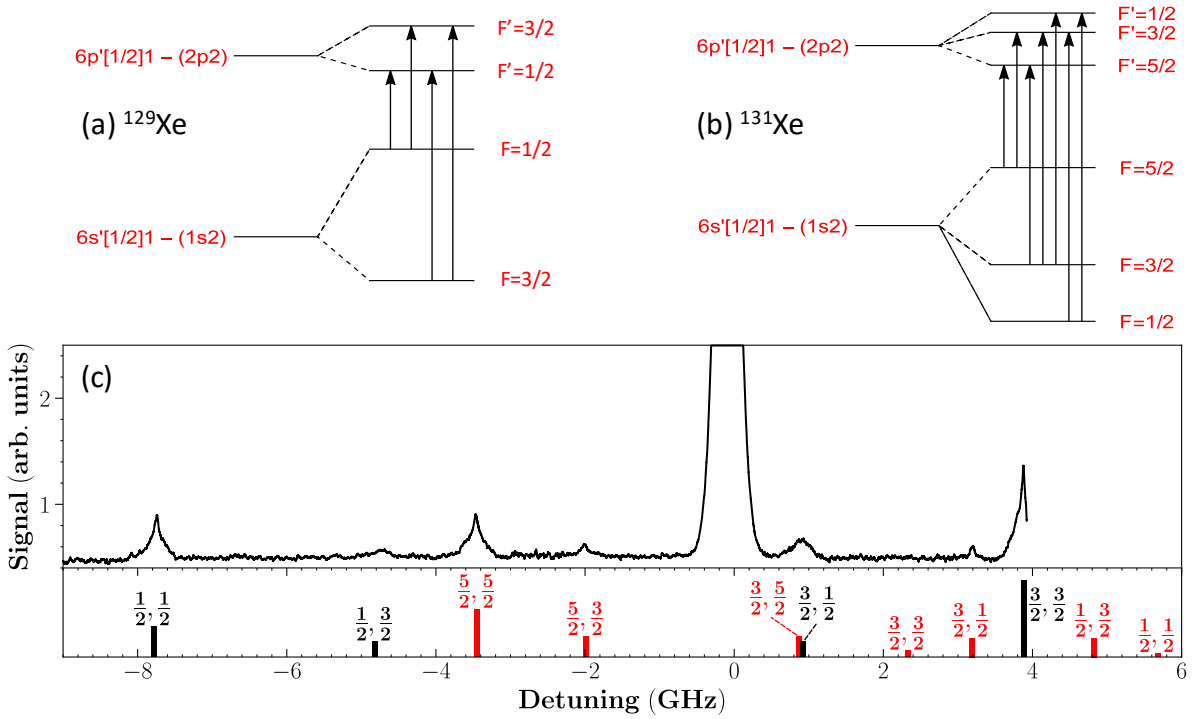

FIG. 5. HFS near 826.879nm for ^{129}Xe and ^{131}Xe: (a),(b) Schematics of the transitions. (c) Experimentally measured saturated absorption spectrum (top plot) and the calculated positions and the strengths of the ^{129}Xe (black) and ^{131}Xe (red) HFS spectral lines (lower plot). The central peak in (c) is due to absorption of the even isotopes, however in this measurement their peaks were not resolved.

Because of the limited scan width for this transition some HFS lines at the right extreme of the tuning range were not observed.

HFS of the $6s[3/2]1 \rightarrow 6p[1/2]0$ transition near 828.239nm

The quantum numbers for this transition are as follows: for ^{129}Xe the lower state corresponds to *J=1, I=1/2* and the upper state to *J=0, I =1/2*; for ^{131}Xe the lower state has *J=1, I=3/2* and the upper state exhibits *J=0, I =3/2*. For this transition the upper level does not have a HFS. Out of total of 5 HFS lines 2 belong to ^{129}Xe and 3 to ^{131}Xe (Fig. 6). From the observed lines the HFS constants can be determined (see Table 1). A reasonable agreement with previous observations [20] is obtained. The peak near zero detuning is due to absorption of the even isotopes.

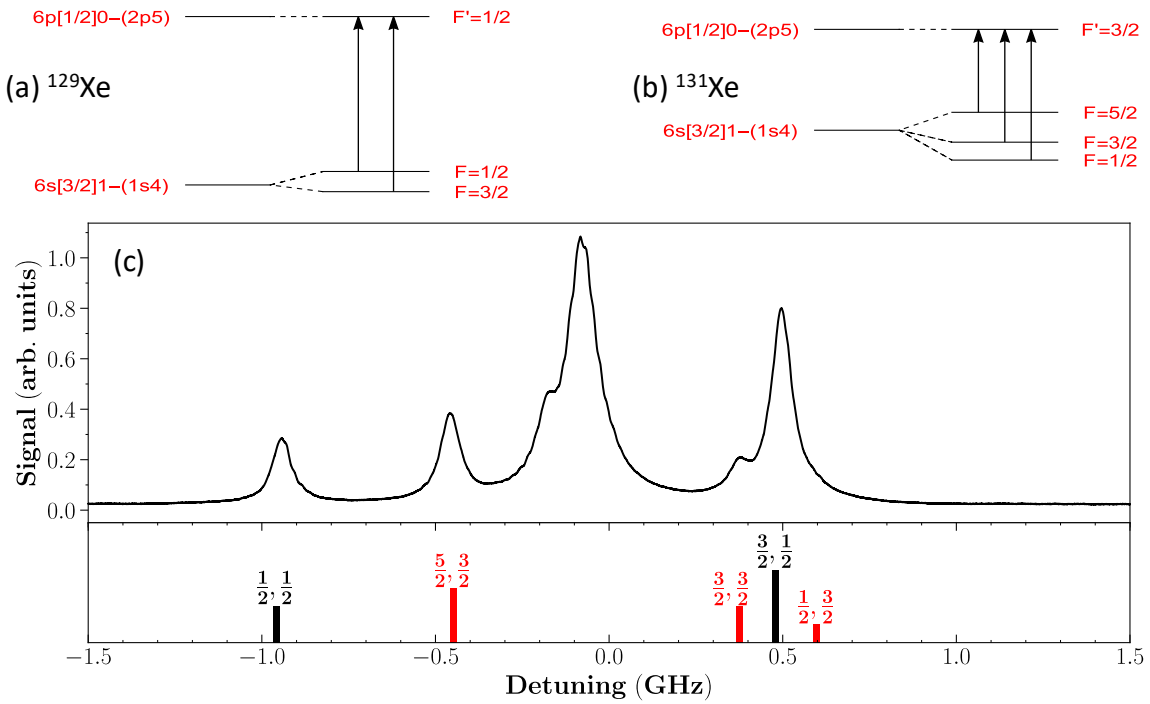

FIG. 6. Characteristics of the $6s[3/2]1 \rightarrow 6p[1/2]0$ transition near 828.239nm: (a),(b) The schemes of the HFS transitions. (c) Measured Xe spectrum and the calculated positions and the strengths of the ^{129}Xe (black) and ^{131}Xe (red) HFS spectral lines (lower plot). The central peak in (c) is due to absorption of the even isotopes, however in this measurement their peaks were not well resolved.

HFS of the $6s'[1/2]1 \rightarrow 6p'[3/2]2$ transition near 834.912nm

The quantum numbers for this transition have the following values: for ^{129}Xe in the lower state *J=1, I=1/2* and in the upper state *J=2, I =1/2*; for ^{131}Xe in the lower state *J=1, I=3/2* and in the upper state *J=2, I =3/2*. The level diagram of the HFS is shown in Fig. 7(a,b), and the measured spectrum is presented in Fig. 7(c). This spectrum was obtained by stitching together two scans.

The transitions measured near 834.912nm required a large dynamic range to observe, as there were large peaks due to the even isotope contributions accompanied by some much smaller hyperfine components. The plot in Fig. 7 is somewhat curtailed on the vertical axis due to excessive gain of the lock-in amplifier, however this large gain allowed observation of the smaller hyperfine contributions. The central peak containing contributions of the even isotopes was saturated at the top and is not fully shown.

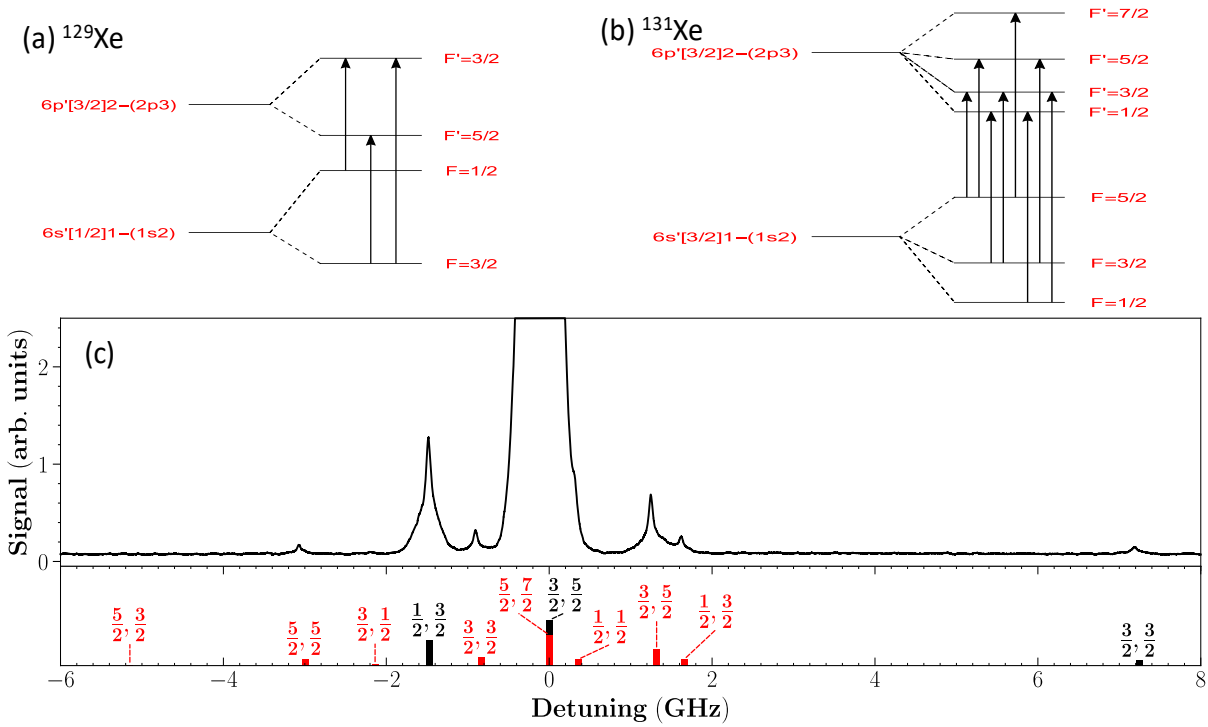

FIG. 7. Data for the $6s'[1/2]1 \rightarrow 6p'[3/2]2$ transition near 834.912nm: (a),(b) The schemes of the HFS transitions. (c) Measured Xe spectrum and the calculated positions and strengths of the ^{129}Xe (black) and ^{131}Xe (red) HFS spectral lines (lower plot). The central peak in (c) is due to absorption of the even isotopes and the indicated transitions of the odd isotopes.

HFS of the $6s[3/2]2 \rightarrow 6p[3/2]1$ transition near 841.150nm

The states of this transition have the following quantum numbers: for ^{129}Xe the lower state has *J=2, I=1/2* and the upper state *J=1, I =1/2*; for ^{131}Xe the lower state has *J=2, I=3/2* and the upper state *J=1, I =3/2*. The level diagram and the measured spectrum are depicted in Fig. 8.

It can be seen that the individual contributions from even isotopes are resolved for transitions near zero detuning, as well as many HFS contributions from the odd isotopes. As with the preceding results, the signals from the even isotopes are large in amplitude compared to the other hyperfine contributions, but they are closely spaced in frequency.

The HFS constants A and B from previous works and the ones obtained by fitting from the data of this work are compiled in Table 1; these constants were used for calculation of the peak positions in the bottom plots of Figs. (3-8). Terms in parenthesis are Paschen notation for the states.

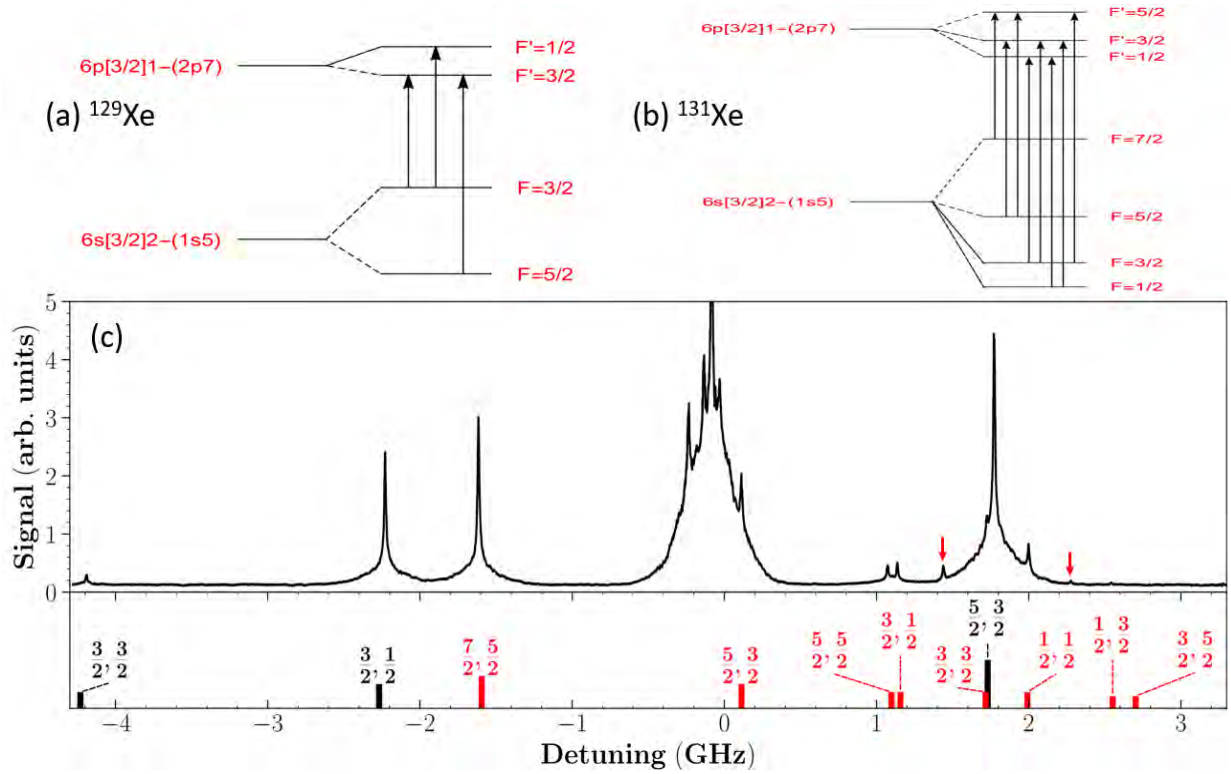

FIG. 8. Data for the $6s[3/2]2 \rightarrow 6p[3/2]1$ transition near 841.150nm: (a,b) Schematics of the HFS transitions. (c) The measured spectrum (upper plot); red arrows indicate peaks that are due to crossover signal artifacts. The enlarged central portion of the plot is shown in Fig. 9(b). The lower plot shows the calculated positions and the strengths of the ^{129}Xe (black) and ^{131}Xe (red) HFS spectral lines.

IV. ISOTOPE SHIFTS

The isotope shift (IS) is given by two contributions: mass shift and field shift. For atoms with intermediate mass, and in particular for Xe, the two contributions are comparable and having opposite signs, they partially cancel each other. Indeed, for Xe rather small ISs were observed for the investigated transitions, where ISs were well resolved. In addition, in spite of the high resolution offered by the Doppler-free technique, the large number of isotopes and the rich hyperfine patterns for some transitions caused overlaps, which obstructed the resolution of separate lines. Also, due to differences in the homogeneous width of the transitions, various saturation intensities and different isotope abundances not all measured transitions allow a clear determination of isotope shifts.

For investigated transitions, we could fully resolve lines of the even xenon isotopes (136, 134, 132, 130, 128) for the transitions near 820.860 nm and 841.150 nm, and for them the IS results are presented in Table II. The weak peaks of ^{124}Xe and ^{126}Xe with low natural abundances could not be observed.

The IS $\Delta\nu$ consisting of the mass shift (MS) $\Delta\nu_M$ and the field shift (FS) $\Delta\nu_F$ (the latter is sometimes referred to also as the volume shift) [33] can be presented as

$$\Delta\nu = \Delta\nu_M + \Delta\nu_F. \quad (8)$$

The mass contribution is commonly presented as a sum of a normal mass shift (NMS) and a specific mass shift (SMS)

$$\Delta\nu_M = \Delta\nu_{NMS} + \Delta\nu_{SMS}. \quad (9)$$

TABLE 1. HFS constants for the states involved in the investigated transitions.

Characteristic wavelength (nm)	Transition states lower/upper	HFS constants (MHz)			References
		A129	A131	B131	
820.860	$6s'[1/2]0$ ($1s_3$)	0	0	0	
	$6p'$ $[3/2]1$ ($2p_4$)	$-4424(1)$	$1321.8(0.9)$	$16.5(0.5)$	[18,19]
		$-4428(5)$	$1310.4(1.9)$	$21(2)$	This work
823.390	$6s[3/2]2$ ($1s_5$)	$-2384.4(1.2)$	$705.4(0.4)$	$255.7(0.6)$	[18,19]
		$-2380(1)$	$708.3(1)$	$246.7(2)$	This work
	$6p[3/2]2$ ($2p_6$)	$-889.6(0.4)$	$262.7(0.4)$	$23.8(0.4)$	[18,19]
		$-891(1)$	$263.9(1)$	$23.7(1)$	This work
826.879	$6s'[1/2]1$ ($1s_2$)	$-5808(2)$	$1709.3(0.7)$	$30.3(0.8)$	[18,19]
		$-5782(4)$	$1710(10)$	$60(20)$	This work
	$6p'[1/2]1$ ($2p_2$)	$1977(1)$	$-581.0(0.6)$	$-6.2(0.4)$	[18,19]
		$1969(6)$	$-590(10)$	$13(10)$	This work
828.239	$6s[3/2]1$ ($1s_4$)	$-959.1(0.7)$	$284.3(0.6)$	$89.9(0.8)$	[18,19]
		$-960(1)$	$290.7(2.4)$	$90.0(1.5)$	This work
	$6p[1/2]0$ ($2p_5$)	0	0	0	
834.912	$6s'[1/2]1$ ($1s_2$)	$-5808(2)$	$1709.3(0.7)$	$30.3(0.8)$	[18,19]
		$-5785(2)$	$1716(1)$	$25.4(3.0)$	This work
	$6p'[3/2]2$ ($2p_3$)	$-2894.6(4.7)$	$858.9(3.1)$	$-14(17)$	[20]
		N/A	$859.4(3.5)$	$3.5(1.0)$	This work
841.150	$6s[3/2]2$ ($1s_5$)	$-2384.4(1.2)$	$705.4(0.4)$	$255.7(0.6)$	[18]
		$-2388(2)$	$705.2(1.8)$	$259(7)$	This work
	$6p[3/2]1$ ($2p_7$)	$-1308.5(4.6)$	$388.9(2.1)$	$10.3(2.6)$	[20]
		$-1308(1.4)$	$384(2)$	$8.8(4.4)$	This work

The calculation of the NMS due to the reduced mass correction is straightforward. For a pair of A and B isotopes with masses M_A and M_B for the transition a with the frequency ν_a

$$\Delta\nu_{NMS}=\nu_a m_e \left(\frac{1}{M_A}-\frac{1}{M_B}\right), \tag{10}$$

where $m_e$is the mass of an electron. The NMS always shifts the heavier isotopes toward larger frequencies, which commonly accepted as a positive IS [34].

The SMS originates from the influence of correlations in the motion of the electrons on the recoil energy of the nucleus. It can be positive or negative depending on the correlations between all the electrons in the atom, and the quantitative theoretical calculation of this contribution is difficult [29]. The SMS can be presented as

$$\Delta\nu_{SMS}=\Delta\nu_{NMS}(K_a\text{-}1), \tag{11}$$

where function K_a depends on the electronic wave functions of the levels involved in the transition [18] and the total MS is then

$$\Delta\nu_M = \Delta\nu_{NMS}\, K_a. \tag{12}$$

The FS is proportional to the field factor F_a and the change of the mean-square nuclear radius for the given isotope pair $\delta < r^2 >_{AB}$:

$$\Delta\nu_F = F_a \delta < r^2 >_{AB}. \tag{13}$$

The variation $\delta < r^2 >_{AB}$ for different isotope pairs can be independently obtained from the data of X-ray isotope shifts, from muonic spectra and electronic scattering experiments [35]. The radii variations are given

relative to ^{136}Xe. Then the MS contribution and the field factor F_a can be extracted by plotting the IS as a function of the radius variation, $\delta < r^2 >_{136,B}$ for different isotope pairs. Namely, if the IS for a given transition is plotted against $\delta < r^2 >_{136,B}$ for the measured isotope pairs, the fitting straight line should have the slope of the field factor, F_a, and the intercept of vertical axis is equal to the MS.

The experimentally observed spectrum with the IS of the even Xe isotopes for the $6s'[1/2]0$ ($1s_3$) → $6p'[3/2]1$($2p_4$) transition near 820.860nm and for the $6s[3\ /\ 2]2 \rightarrow 6p[3\ /\ 2]1$ transition near 841.150nm are shown in Fig. 9. We observed that the resolving of five peaks of the even isotopes strongly depends on the intensity, since excessive intensity can lead to signal saturation, but when it is too low the signal is weak.

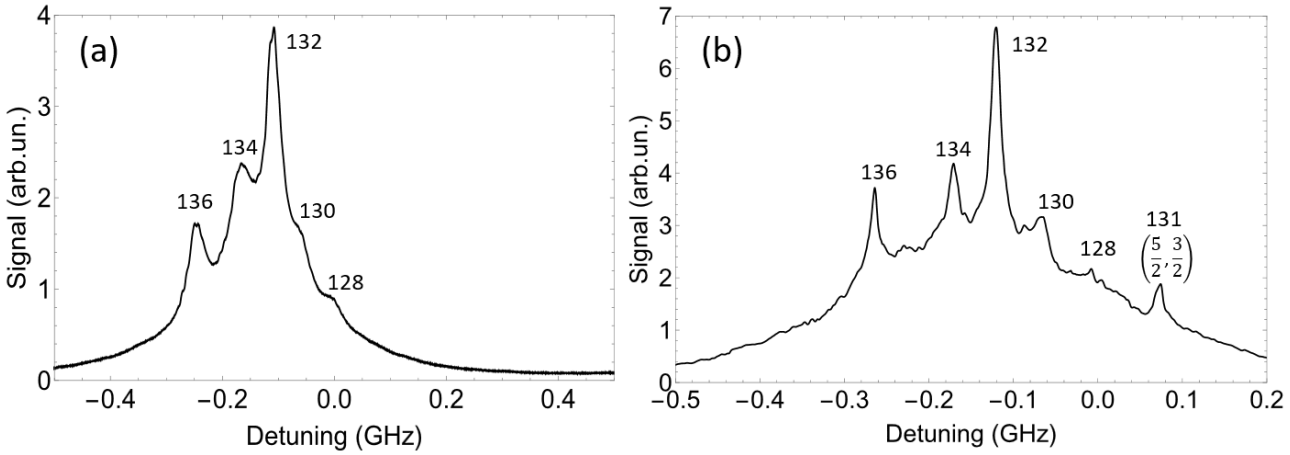

FIG. 9. Absorption peaks of the even isotopes in the enlarged portions of the scans from Fig. 3 and Fig. 8, respectively: (a) For the $6s'[1/2]0 \rightarrow 6p'[3/2]1$($2p_4$) transition near 820.860nm; (b). For the $6s[3\ /\ 2]2 \rightarrow 6p[3\ /\ 2]1$ transition near 841.150nm.

The experimental ISs are presented in Table II and compared to values from Ref. [20]. The consistency of the data and the model can be checked with the King-plot analysis [18]. This plot presents the IS of transition b as a function of the IS of transition a for each measured isotope pair. With the model of Eqs. (8-13) this dependence should be a straight line with the slope equal to the ratio of the field factors of the transitions,

TABLE II. The observed isotope shifts $\Delta\nu$ of xenon stable isotopes (in MHz)*).

Transition	Transition wavelength	Isotope pair	$\Delta\nu$, this work	$\Delta\nu$, Ref. [20]
$6s'[1/2]0(1s_3)\rightarrow$ $6p'[3/2]1(2p_4)$	820.860nm	136-134	-80.9(2.0)	-76.4 (4.7)
		136-132	-132.4(2.1)	-129.0 (5.7)
		136-131	-203.0(3.6)	-197.4(7.4)
		136-130	-181.9(5.3)	-189.1 (11.0)
		136-129	-240.0(3.2)	-238(5.0)
		136-128	-242.4(2.4)	-250.3 (8.2)
$6s[3/2]2(1s_5) \rightarrow$ $6p[3/2]1(2p_7)$	841.150nm	136-134	-94.9(3.9)	-97.2 (4.4)
		136-132	-147.3(4.4)	-151.8 (5.3)
		136-131	-222.2(7.1)	−229.2 (4.7)
		136-130	-199.7(4.5)	-209.5 (6.9)
		136-129	-274.8(4.9)	−272.6 (5.1)
		136-128	-261.2(4.8)	-269.3 (7.4)

*) The ISs for the odd isotopes were determined from the positions of the centroids calculated using Eq. (7).

F_b/F_a and the intercept equal to $\left[(\Delta\nu_b - \Delta\nu_a\left({}^{F_b}/_{F_a}\right)\right]$. As transition a we take $6s'[1/2]0$ ($1s_3$) $\rightarrow$ $6p'[3/2]1$ ($2p_4$), and as transition b we take $6s[3/2]2(1s_5) \rightarrow 6p[3\ /\ 2]1\ (2p_7)$. Using data of Ref. [32] for the charge radii, we have determined F_a=33147 Hz/fm^2 and F_b=32426 Hz/fm^2, and thus, F_b/F_a=0.978. From the King-plot with the data for these two transitions we find a very close value $F_b/F_a = 0.977$, which shows that our data are indeed consistent.

V. SIMULATION OF THE OBSERVED SIGNAL PROFILES

We use a simple model to simulate the observed shapes of the saturated absorption signals [36]. The inhomogeneously broadened absorption profile is described as $\gamma(\nu) = \gamma_0 \exp\left[-(\nu-\nu_0)^2/(\Delta\nu_D)^2\right]$, where $\Delta\nu_D$ is the width due to Doppler broadening and ν_0 is the center of this absorption profile, which in further consideration we set to zero, $\nu_0 = 0$. The homogeneous absorption line shape of the transition can be described as $g(\nu, \nu', \Delta\nu) = \Delta\nu/\{2\pi[(\nu-\nu')^2 + (\Delta\nu/2)^2]\}$ for a class of molecules having velocity projection on the light propagation direction, such that the resonance frequency is ν'. The inhomogeneous absorption profile accounting for the saturation is given by [36]

$$\gamma_s(\nu) \propto \int_{-\infty}^{\infty} p(\nu')\ g(\nu, \nu', \Delta\nu_s)\, d\nu', \tag{14}$$

where $p(\nu')d\nu'$ is the probability that the atom has its resonance frequency between ν' and $\nu' + d\nu'$; $\Delta\nu_s = \Delta\nu[1 + I(\nu)/I_s]^{1/2}$ is the line width modified by the saturation effect, $I(\nu)$ is the spectral intensity and I_s is the saturation intensity. For $\Delta\nu_D \gg \Delta\nu_s$ the probability $p(\nu) \propto \gamma(\nu)$. The expression for $\gamma_s(\nu)$ can be presented in a form

$$\gamma_s\big(\nu, I(\nu)\big) = \frac{\Delta\nu}{2\pi}\int_{-\infty}^{\infty} \frac{\gamma(\nu')d\nu'}{(\nu-\nu')^2 + (\Delta\nu/2)^2[1 + I(\nu)/I_s]}\,. \tag{15}$$

Here the factor $\Delta\nu/2\pi$ is the normalization factor such that in the limiting case $\gamma_s \rightarrow \gamma(\nu)$ for small intensities, when $I(\nu)/I_s \rightarrow 0$. The detected signal S is proportional to the difference of the transmitted light when the pump is on and off. We assume that the initial intensity of the laser beam $I(\nu) = I_0(\Delta\nu_L)^2/(\nu^2 + (\Delta\nu_L)^2)$ is split between the probe $I_{probe}(\nu) = K\, I(\nu)$ and the pump $I_{pump}(\nu) = (1-K)I(\nu)$ beam intensities, as determined by the coefficient K. When the pump is off, a partial saturation is occurring due to the probe beam (which is always "on"), since in this case the intensity is $I_1 = KI(\nu)$. When the pump is also on, the peak intensity is $I_2 = KI(\nu) + (1-K)I(-2\nu)$, here we take $I(-2\nu)$, since the pump beam propagates in the opposite direction compared to the probe beam and interacts with the same class of molecules as the probe beam when the frequency is shifted by (-2ν) due to the Doppler effect. Further we assume that when the laser scans the frequency and the signal is recorded, the peak intensity does not change. Consequently, the following expression can be used

$$S(\nu) \propto (\,I(\nu)/I_s)[\exp(-\gamma_s(\nu, I_2\,)x) - \exp(-\gamma(\nu, I_1)x)]\,, \tag{16}$$

where x is the propagation distance in the gaseous sample, and it is assumed that the detector output is proportional to the incident intensity. This expression was calculated for different values of the parameters (Fig. 10). With the reduction of the homogeneous linewidth, $\Delta\nu$, the central portion of the signal profile becomes narrower and its amplitude reduces, while the wings preserve relatively large width (Fig. 10(a)). The variation of the K parameter, which determines the portion of the total intensity that is used in the probe beam shows that for a given intensity I_0 the optimal signal tends to increase as K approaches $K \sim 0.5$ (Fig. 10(b)). As the optical density of the sample increases $(\gamma_0 x) \geq 1$, the calculations should be performed taking into

account the variation of intensity from one layer of the sample to the next one, as the beams propagate in the absorbing medium. Since the pump beam is counterpropagating the probe beam its intensity is increasing in the direction of the probe beam propagation. With the initial increase of the $(\gamma_0 x)$ value the effect of the saturation becomes more pronounced and the signal increases too (Fig. 10(c)), however at large $(\gamma_0 x)$ values and fixed intensity the signal diminishes with further increase of this parameter (Fig. 11(a)), since lower intensity is transmitted through the sample. Also, the wings of the signal profile become more pronounced compared to its central part. The depend of the signal amplitude $S(0)$ on the normalized pump intensity (I_0/I_s) is depicted for three values $(\gamma_0 x)$ =1,5,10 in (Fig. 11(b)). For $(\gamma_0 x) = 1$ the signal initially quickly increases with the intensity and then at $(I_0/I_s) \gg 1$ experiences saturation. For a higher optical density of the sample $(\gamma_0 x) = 5{,}10$ the initial increase of the signal is much slower, however with the increase of the intensity, the saturation effect is less and consequently the signal becomes larger.

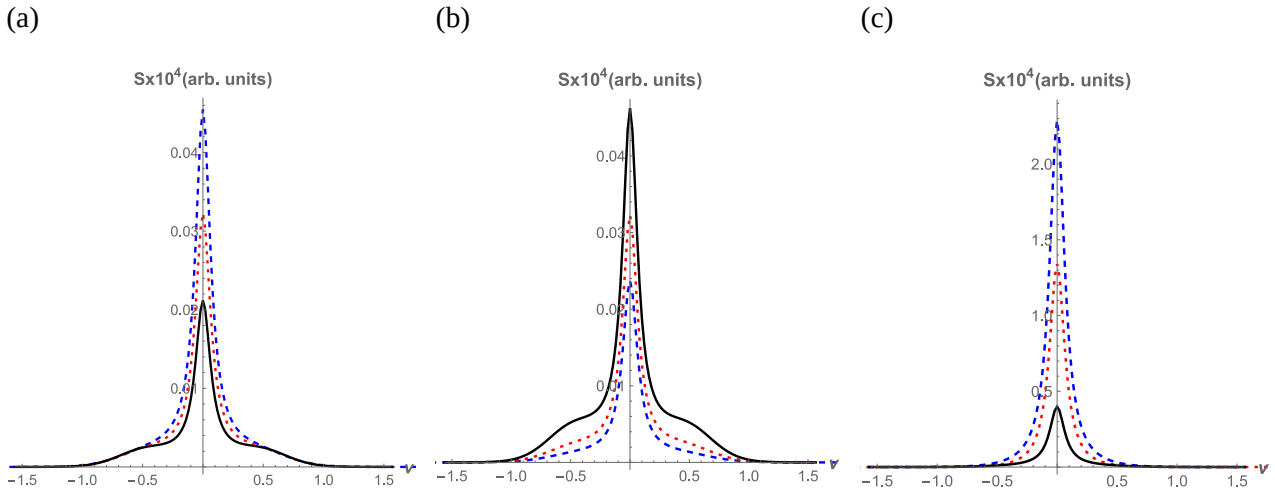

Fig. 10. Simulated saturated absorption spectroscopy signals in the vicinity of the absorption peaks vs. frequency for: (a) the variation on the $\Delta\nu$ (dashed blue line for $\Delta\nu = 0.3$, dotted red line for $\Delta\nu = 0.2$ and solid black line for $\Delta\nu = 0.1$); (b) the variation on the K parameter (dashed blue line for $K = 0.1$, dotted red line for $K = 0.2$ and solid black line for $K = 0.5$; (c) the variation on the $(\gamma_0 x)$ dimensionless parameter (dotted red line for $\gamma_0 x = 0.2$, dashed blue line for $\gamma_0 x = 1$ and solid black line for $\gamma_0 x = 3$. In 5) calculations the values of parameters unless changed as indicated above were: $\Delta\nu = 0.3, \Delta\nu_L = 0.3, I_0/I_s = 0.1, \gamma_0 x = 5, K = 0.2$.

The line profiles with sharp central peaks and broad wings at the base were observed in many measured spectra (see Figs. (3,4,8)). The suppression of the central part of the absorption lines of the even isotopes observed at ~823 nm can likely be attributed to the high optical density of the Xe sample, since similar profiles can be seen in Fig. 11(a).

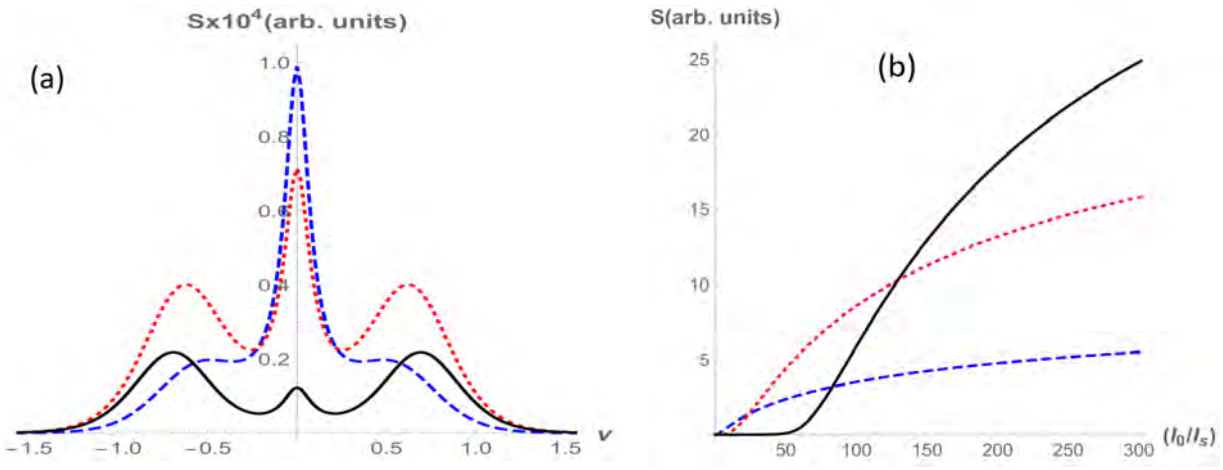

Fig. 11. Simulations of the signal at the parameter values $K = 0.2, \Delta\nu = 0.3, \Delta\nu_L = 0.3$: (a) the variations of the signal shape for large optical densities of the sample: dashed blue line for $\gamma_0 x = 8$, dotted red line for $\gamma_0 x = 10$ and solid black line for $\gamma_0 x = 12$, $I_0/I_s = 2$ (the S values for the last two lines are magnified ×5). (b) The dependence of the signal amplitude $S(0)$ on the normalized pump intensity for $\gamma_0 x = 1$ (dashed blue line), for $\gamma_0 x = 5$ (dotted red line) and for $\gamma_0 x = 10$ (solid black line).

VI. CONCLUSIONS

The xenon atom with nine stable isotopes is of high interest for applied research as well as for fundamental studies with high sensitivity and high-resolution laser spectroscopic techniques. The hyperfine structure and isotope shifts of Xe isotopes were observed for several transitions in the near-IR range 820-841 nm by using the Doppler-free saturated absorption spectroscopy approach. The absorption lines were measured in an inductively coupled Xe discharge. We were able to identify wavelength regions (around 820.860nm and 841.150nm) where transitions for seven different Xe isotopes could be clearly observed. Furthermore, the positions of the HFS lines are in good agreement with previous measurements by other groups, and the shapes of these lines have been simulated with numerical models. Overall, from the point of view of isotope identification by their HFS profiles, the transitions at around 820.860nm, 823.390nm and 841.150nm look most promising, since they provide many characteristic HFS lines. For transitions near 820.634 nm and 841.150nm also well resolved absorption peaks of even isotopes were observed that can be identified by their isotope shifts. Applying this method to optical absorption measurements shows promise of performing quantitative isotopic abundance measurements, including measurement of different isomers of the same isotope. Further development of this approach can be used for designing a compact apparatus of Xe isotope analysis.

ACKNOWLEDGMENTS

This work was supported by the subcontract STL-007-21 sponsored by the DOE and by the grant A1546 from the Robert Welch Foundation.

REFERENCES

1. Gordon K. Woodgate, Elementary Atomic Structure. Oxford University Press, 1999.
2. T. W. Haensch, A. L. Schawlow, and G. W. Series. The spectrum of atomic hydrogen. Scientific American, 240, 72 (1979).
3. R. A. McFarlane, W. R. Bennett Jr, W. E. Lamb Jr, Single mode tuning dip in the power output of an he-ne optical maser, Appl. Phys. Lett. 2, 189 (1963).
4. CRC Handbook of Chemistry and Physics, 80th ed.; Lide, D. R., Ed.; CRC Press: Boca Raton, FL, 1999.
5. P. R.J. Saey, Xenon, In: Radionuclides in the Environment. Edited by David A. Atwood. John Wiley & Sons, 2010, pp.179-189.
6. R. A. Fish and G. G. Goles, Ambient xenon: A key to the history of meteorites. Nature 196, 27-31 (1982).
7. G. Avice, B. Marty and R. Burgess, The origin and degassing history of the Earth's atmosphere revealed by Archean xenon, Nature Communications, 8, 15455 (2017).
8. E. Esencan, S. Yuksel, Y. B. Tosun, A. Robinot, I. Solaroglu and J. H. Zhang, Xenon in medical area: emphasis on neuroprotection in hypoxia and anesthesia, Medical Gas Research, 3, 4 (2013).
9. C.C. Lu et al., Relativistic Hartree-Fock-Slater eigenvalues, radial expectation values, and potentials for atoms $2 < Z < 126$, Atomic data 3, 1-131 (1971).
10. G. A. Canella, R. T. Santiago, R. L.A. Haiduke, Accurate determination of the nuclear quadrupole moment of xenon from the molecular method, Chemical Physics Letters, 660, 228-232 (2016).
11. W. Makulski, Explorations of magnetic properties of noble gases: the past, present, and future, Magnetochemistry, 6, 65 (2020).
12. D. A. Jackson, a n d M.-C. Coulombe, Isotope shifts in the arc spectrum of xenon, Proc. R. Soc. Lond. A. 338, 277-298 (1974).
13. W. Fischer, H. Huehnermann, G. Kroemer, and H.J. Schaefer, Isotope Shifts in the Atomic Spectrum of Xenon and Nuclear Deformation Effects, Z. Physik 270, 113 - 120 (1974).
14. Q. L. Faust AND M. N. McDermott, Hyperfine structure of the $(5p)^5(6s)\ ^3P_2$ state of $_{54}Xe^{129}$ and $_{54}Xe^{131}$, Phys. Rev. 123, 198-204 (1961).
15. W. Borchers, E. Arnold l, W. Neu, R. Neugart, K. Wendt, G. Ulm, Xenon isotopes far from stability studied by collisional ionization laser spectroscopy, Phys. Lett. B, 216, 7-10 (1989).
16. X. Li, J. Lassen and H. Schuessler, High-efficiency ultra trace detection of 85Kr, Proc. SPIE 4634, Methods for Ultrasensitive Detection II, (28 March 2002);
17. N. Beverini, G. L. Genovesi and F. Strumia, Xenon saturation spectroscopy by diode laser, IL Nuovo Cimento, 17 D, 515-522 (1995).
18. G. D'Amico, G. Pesce and A. Sasso, Isotope-shift and hyperfine-constant measurements of near-infrared xenon transitions in glow discharges and on a metastable Xe ($^3P_2$) beam, Phys. Rev. A 60, 4409-4416 (1999).
19. G. D'Amico, G. Pesce and A. Sasso, High resolution spectroscopy of stable xenon isotopes, Hyperfine Interactions 127, 121–128 (2000).
20. M. Suzuki, K. Katoh, N. Nishimiya, Saturated absorption spectroscopy of Xe using a GaAs semiconductor laser, Spectrochimica Acta Part A, 58 2519–2531 (2002).
21. E. Pawelec, S. Mazouffre, N. Sadeghi, Hyperfine structure of some near-infrared Xe I and Xe II lines, Spectrochimica Acta Part B: Atomic Spectroscopy, 66, 470-475 (2011).
22. A. Kuwahara, Y. Aiba, S. Yamasaki, T. Nankawad and M. Matsui, High spectral resolution of diode laser absorption spectroscopy for isotope analysis using a supersonic plasma jet, J. Anal. At. Spectrom., 33, 1150 (2018).

23. G. T. Hickman, J. D. Franson, and T. B. Pittman, Optically enhanced production of metastable xenon, Optics Letters, 41, 4372-4374 (2016).
24. G.N. Malović, A.I. Strinić, Z.Lj. Petrović, J.V. Božin, and S.S. Manola, Electron excitation coefficients for 2p and 3p levels of Xe, Eur. Phys. J. D 10, 147–151 (2000).
25. L. Allen, D. G. C. Jones, and D. G. Schofield, Radiative Lifetimes and Collisional Cross Sections for Xe i and ii, JOSA, 59, 842-847 (1969).
26. E.W. Otten, Hyperfine Interactions 2, 127-149 (1976).
27. H.-J. Kluge, Optical Spectroscopy of Short-Lived Isotopes, in: Progress in Atomic Spectroscopy B. W. Hanle and H. Kleinpoppen, Eds. (Plenum Press, New York, 1978), p. 727.
28. R. Neugart and G. Neyens: Nuclear Moments, Lect. Notes Phys. 700, 135–189 (2006).
29. H. Kopfermann and E.E. Schneider, Nuclear moments (Academic Press, 1958).
30. R. D. Cowan, The Theory of Atomic Structure and Spectra (Berkeley, CA: Univ. California Press, 1981).
31. G. M. Wahlgren, D. S. Leckrone, S. G. Johansson, M. Rosberg and T. Brage, The abundances of Pt, Au, and HG in the chemically peculiar HgMn-type stars kappa CANCRI and chi LUPI, Astrophys. J., 444, 438-451 (1995).
32. M. Ding and J. C. Pickering, Measurements of the Hyperfine Structure of Atomic Energy Levels in Co II, Astrophys. J., Suppl. Ser., 251, 24 (2020).
33. K. Heilig and A. Steudel, Changes in mean-square nuclear charge radii from optical isotope shifts, Atomic data and nuclear data tables 14, 613-638 (1974).
34. G. Fricke, C. Bernhardt, K. Heilig, L.A. Schaller, L. Schellenberg, E.B. Shera, C.W. Dejager, Nuclear Ground State Charge Radii from Electromagnetic Interactions, Atomic Data and Nuclear Data Tables,60 (2), 177-285 (1995).
35. I. Angeli and K.P. Marinova, Table of experimental nuclear ground state charge radii: An update, Atomic Data and Nuclear Data Tables, 99(1), 69-95 (2013).
36. A. E. Siegman, Lasers (University Science Books, Mill Valey, California, 1986), chapter 30.